ORIGINAL CONTRIBUTION: QUANTIFICATION OF VAPORIZED TARGETED NANODROPLETS USING HIGH FRAME RATE ULTRASOUND AND OPTICS

GE ZHANG*, SHENGTAO LIN*, CHEE HAO LEOW*, KUIN TIAN PANG†, JAVIER HERNÁNDEZ-GIL§, NICHOLAS LONG§, ROBERT ECKERSLEY‡, TERRY MATSUNAGA‡, and MENG-XING TANG*

* Department of Bioengineering, Imperial College London, United Kingdom

† Institute of Molecular and Cell Biology, Agency for Science, Technology and Research (A*STAR), Singapore

§ Department of Chemistry, Imperial College London, United Kingdom

‡ Division of Imaging Sciences & Biomedical Engineering Department, King's College London, United Kingdom

‡ Department of Medical Imaging, University of Arizona, United States of America

Address correspondence to: Meng-Xing Tang, Department of Bioengineering, Imperial College London, United Kingdom, SW7 2AZ, Tel: +44 207 5943664. E-mail: mengxing.tang@imperial.ac.uk

Abstract- Molecular targeted nanodroplets, promising to extravasate beyond the vascular space, have great potential to improve tumor detection and characterization. High frame rate ultrasound, on the other hand, is an emerging tool for imaging at a frame rate 1-2 orders of magnitude higher than common existing ultrasound operating systems. In this study, we used high frame rate ultrasound combined with optics to study the acoustic response and size distribution of Folate Receptor (FR) - targeted versus Non-Targeted (NT)-nanodroplets *in vitro* with MDA-MB-231 breast cancer cells immediately after ultrasound activation. A flow velocity mapping technique, Stokes' theory, and optical microscopy were used to estimate the size of both floating and attached vaporized nanodroplets immediately after activation. It was found that the size of floating vaporized nanodroplets was on average more than 7 times larger than the size of vaporized nanodroplets attached to the cells. The results also showed that the acoustic signal of vaporized FR-nanodroplets was persistent after activation, with 70% of the acoustic signals still present 1 second after activation, compared to the vaporized NT-nanodroplets where only 40% of the acoustic signal remains. The optical microscopic images showed on average 6 times more vaporized FR-nanodroplets generated with a wider range of diameters (from 4 to 68 µm) that still attach to the cells compared to vaporized NT-nanodroplets (from 1 to 7 µm) with non-specific binding after activation. It was also found that the mean size of attached vaporized FR-nanodroplets was on average about 3-fold larger than that of attached vaporized NT-nanodroplets. The study offers an improved understanding of the vaporization of the targeted nanodroplets in terms of their sizes and acoustic response in comparison with non-targeted ones, taking advantage of high-frame-rate contrast-enhanced ultrasound and optical microscopy. Such understanding would help design optimized methodology for imaging and therapeutic applications.

Key words: **Targeted Molecular Imaging, Nanodroplets, Phase-Change Contrast Agents, Microbubbles.**

INTRODUCTION

Medical ultrasound imaging has been regarded as a highly accessible and affordable tool that can provide high-resolution and real-time images without any ionising radiation. The advent of contrast-enhanced ultrasound (CEUS) with microbubble contrast agents, together with the development of contrast specific pulse sequences have significantly increased imaging sensitivity from within the blood (Eckersley, et al. 2005). Furthermore, the microbubbles have also been used in ultrasound-mediated therapies as well (Dijkmans, et al. 2004). Recently the field has seen new developments in high-frame-rate CEUS imaging (Leow, et al. 2015, Tremblay-Darveau, et al. 2014).

It has been demonstrated that low-boiling-point perfluorocarbon nanodroplets can be formed simply by condensing their perfluorocarbon microbubbles with increasing pressure and decreasing temperature (Sheeran, et al. 2011). These low-boiling-point nanodroplets can be rapidly activated to microbubbles by the application of external acoustic pressure, commonly referred to as 'acoustic droplet vaporisation (ADV)' (Kripfgans, et al. 2000). These nanodroplets mainly have three advantages compared to micorbubbles in the context of CEUS imaging applications. First, nanodroplets have smaller diameters than microbubbles which enables them to potentially go beyond the vascular region not accessible to microbubbles. Second, nanodroplets have longer half-life than microbubbles under in vivo conditions. Third, nanodroplets can be activated into microbubbles in any preset time and location (Sheeran and Dayton 2014). Such features of nanodroplets have enabled their applications for super-resolution imaging (Zhang, et al. 2018, Zhang, et al. 2018), dual-modality imaging (Lin, et al. 2017), High Intensity Focused Ultrasound (HIFU), therapeutic histotripsy (Aydin, et al. 2016, Moyer, et al. 2015), sonoporation (Liu, et al. 2016), chemotherapy (Zhu, et al. 2017) and drug & gene delivery (Zhou, et al. 2014). In biology and tissue engineering, nanodroplets can also be used for DNA fragmentation (Kasoji, et al. 2015) and acoustically responsive scaffolds (Moncion, et al. 2016) where microbubble contrast agents cannot.

In cancer imaging and therapy, nanodroplets could play an important role as they are approximately 3 to 6 times smaller in diameter than microbubbles prior to vaporisation theoretically (Mercado, et al. 2016, Oleksandr, et al. 2013) and approximately 12 fold smaller in diameter experimentally (Sheeran, et al. 2015). These nanodroplets have the potential to extravasate from the vascular endothelium to the cancerous tissue and form target-specific binding. Once bound, the targeted nanodroplets can be vaporized into microbubbles for imaging and therapeutic purposes. The maximum particle extravasation size from the vasculature is approximately 10 nm in normal tissue whereas the gap junction between the porous tumour endothelium may be as large as 200 nm (Ji, et al. 2013). The enhanced permeability and retention (EPR) effect increases the passive accumulation of nanoparticles (50-200nm) in tumour tissue. It has been found that the nanodrug delivery to tumors by the EPR effect can only offer a 2-fold improvement in nanodrug delivery compared with normal tissue, which results in insufficient drug concentration for treating most cancers (Nakamura, et al. 2016). With respect to cancer, it has been found that the folate-receptor (FR) is overexpressed on the surface of breast, ovarian, cervical, and colorectal cancer cells but not in normal human tissue (Parker, et al. 2005). Previous literature has reported the treatment of ovarian cancer in Phase II clinical trials using a FR-targeted chemotherapeutic agent combined with FR-targeted SPECT imaging agents (Morris, et al. 2014, Naumann, et al. 2013). In addition, recent work (Hadinger, et al. 2018, Marshalek, et al. 2016) using FR-targeted nanodroplets has demonstrated that targeted agents can also selectively promote intracellular delivery which can be incorporated as a strategy for using nanodroplets for even more precise cancer cell imaging and therapy (Matsunaga, et al. 2012).

The low-boiling-point decafluorobutane nanodroplets (boiling point = - 2ºC) have been investigated for imaging purposes (Zhang, et al. 2018, Zhang, et al. 2017). The first ultrasound molecular imaging using low-boiling-point nanodroplets was demonstrated in 2013 (Sheeran, et al. 2013). As proof-of-principle, Sheeran and co-workers used RGD peptide-targeted nanodroplets to target the overexpressed $\alpha_v\beta_3$ integrin on human umbilical vein endothelial cells. However, this

study was performed using a clinical Siemens imaging systems and therefore the imaging frame rate was limited to 30 Hz. Using confocal microscopy, Marshelek et al. have shown the capability of low-boiling-point FR-nanodroplets to target MDA-MB-231 breast cancer cells followed by internalisation via folate-receptor mediated endocytosis (Marshalek, et al. 2016). However, some important aspects of the targeted nanodroplet immediately after vaporisation, including the acoustic response and size distribution of the resultant microbubbles have not been fully understood.

In this study, we investigated the acoustic response and size distribution of vaporized folate-receptor targeted nanodroplets with MDA-MB-231 breast cancer cells using high frame rate ultrasound and optics. The study offers an improved understanding of the vaporization of the targeted nanodroplets in terms of their sizes and acoustic response in comparison with non-targeted ones, taking advantage of high-frame-rate contrast-enhanced ultrasound and optical microscopy. Such understanding would help design optimized methodology for imaging and therapeutic applications.

MATERIALS AND METHODS

Preparation & Characterization of Nanodroplets

Preparation of nanodroplet solutions was adapted from previously described methods (Marshalek, et al. 2016). For the non-targeted (NT) -nanodroplet lipid solution, the lipid colloid was generated by dissolving a 9:1 molar ratio of 1,2-dipalmitoyl-sn-glycero-3-phosphocholine (DPPC) and 1,2-distearoyl-sn-glycero-3-phosphoethanolamine-N-[amino(polyethylene glycol)-2000] (DSPE-PEG-2000) into a solution of phosphate-buffered saline (PBS), propylene glycol, and glycerol (16:3:1, volume: volume) to achieve a total lipid concentration of 1 mg/mL (Avanti Polar Lipids, Alabaster, AL, USA). For the FR-targeted lipid solution (FR-nanodroplets), 1,2-distearoyl-sn-glycero-3-phosphoethanolamine-N-[folate(polyethylene glycol)-2000] (DSPE-PEG-2000-Folate) was added to the mixture of lipid powder to maintain a 9:0.8:0.2 molar ratio of DPPC, DSPE-PEG-2000, and DSPE-PEG-2000-Folate respectively. The mixture of lipid powder was also dissolved

into a solution of PBS, propylene glycol, and glycerol (16:3:1, volume: volume) to achieve a total lipid concentration of 1 mg/mL (Avanti Polar Lipids, Alabaster, AL, USA). The DSPE-PEG-2000-Folate lipid bioconjugate was prepared following a previous described method (Chen, et al. 2013). A volume of 1 mL of lipid solution was added to a 2 mL glass vial.

The headspace of the vial was purged with decafluorobutane gas (Fluoromed, Round Rock, TX, USA) via an inlet needle and the contents equilibrated with a vent needle. Mechanical agitation was applied using a modified amalgamator (Bristol-Myers-Squibb, New York, NY, USA) to produce the stable microbubbles.

For condensing microbubbles into nanodroplets, the headspace of the vial was pressurised according to previous methods (Zhang, et al. 2018). Briefly, the vials of microbubbles were immersed in an ice-salt bath (-5 ℃ to-10 ℃) followed by pressurization with ambient air into the vial septum.

A NanoSight NS300 (Malvern Instruments, Inc., Malvern, UK) was used to measure the size and concentration of both FR- and NT-nanodroplet solutions via nanoparticle tracking analysis (NTA); the nanoparticle measurement range being 10 nm to 1000 nm. Both nanodroplet solutions were diluted 1000-fold in deionised water. Three (3) samples were prepared for each nanodroplet solution and 3 measurements were performed for each sample. For both FR- and NT-nanodroplet solutions, 9 measurements in total (N=9) were performed to obtain the mean values of size and concentration of each nanodroplet solution. Five vials of nanodroplet solution were consolidated to form the final nanodroplet solution for the experiments.

Cell culture

The immortalised human breast cancer cell line, MDA-MB-231, was obtained from an immortalized cell line maintained at the Hammersmith Hospital campus at Imperial College London. Cells were grown in RPMI-1640 Medium supplemented with 10% fetal bovine serum (FBS), 2mM L-glutamine, 100 U/mL penicillin and 100μg/mL streptomycin (Sigma-Aldrich, St. Louis, Missouri,

USA). Cells were cultured in a T75 culture flask at 37 ℃ in an incubator with 5% CO_2. The mean diameter of the cells were about 20-30 μm as noted by prior literature (Kim, et al. 2007).

Experimental set-up

MDA-MB-231 cells were detached with 0.25% trypsin-ethylenediaminetetraaceticacid (EDTA) (Sigma-Aldrich, Missouri, USA). Detached cells were neutralised using full serum media and centrifuged at 1300 rpm for 5 minutes. Cell pellets were resuspended in 1 mL of media before seeding 2.2 million cells with 10 mL of media into an optically and acoustically transparent Opticell chamber (Nalge Nunc International, Rochester, USA). The inner dimensions of the Opticell chamber are 7.6 cm x 6.6 cm x 0.2 cm respectively. The thickness of the MDA-MB-231 breast cancer cell layer is normally about 5 μm according to previous literature (Winnard, et al. 2008). After 24 hours of incubation, 0.2 mL of nanodroplet solution (~ 1.1×10^9 nanodroplets) were added to the media and the diluted solution mixed well before being injected into each Opticell chamber. The chamber was incubated at 37℃ for 10 minutes. After incubation, media was aspirated and cells were washed with additional media three times to remove any residual unbound nanodroplets from the Opticell Chamber. The Opticell chamber was then immersed and equilibrated in a 37℃ temperature-controlled water tank. The transducer was held 15mm above the top surface of the Opticell chamber as illustrated in Figure 1. Acoustic absorbers were placed at the bottom of the water tank to reduce ultrasound reflection. Immediately after the acquisition of ultrasound data, the Opticell chambers were transferred to obtain the microscopic imaging. Images were obtained using a Nikon DXM-1200C (Nikon Instruments Inc.) equipped with a 40× objective lens and a numerical aperture (NA) of 0.65. The resolution of the microscope is 0.1613 μm/pixel. The microscopic imaging plane was focused directly on the breast cancer cells fixed to the bottom plane of the Opticell chamber. As a reference point for microscopic imaging, the Opticell chamber under the transducer where ultrasonic activation conducted was marked. For each Opticell chamber, five independent optical measurements in different regions were acquired before and after ultrasound

exposure to observe the newly vaporized nanodroplets attached to the cell surface. Two Opticell chambers were used for FR- nanodroplets and another two for NT- nanodroplets.

Imaging Acquisition & Analysis

A customised 'Imaging-Activation-Imaging' acquisition sequence as demonstrated in Table 1 was implemented on an ultrasound research platform (Verasonics Vantage 128, Kirkland, USA) with a L11-4 38-mm linear array probe (ATL, USA) (Lin, et al. 2016). The spatial and temporal peak-negative-pressure (PNP) was measured by hydrophone calibration as described by Lin (Lin, et al. 2017). The acoustic vaporisation of nanodroplets were achieved by electronically sweeping of the transmitted focus waves (8-MHz, 5-cycle sinusoidal waves with peak negative pressure of 5.37 MPa, f-number=0.4, axial focus=15 mm) over the depth of interest. Only one activation focus-pulse was transmitted to activate the nanodroplets. For imaging, a coherent compounding plane wave pulse inversion technique was employed to form an image (Montaldo, et al. 2009). Plane waves were transmitted at 9 different angles (Angle range: -10° to 10°) at 4 MHz with a PNP of 0.20 MPa was transmitted. The ultrasound imaging resolution cell size was 0.56 x 0.64 x 1.5 mm respectively in the axial, lateral and elevational directions. Similar to conventional pulse inversion technique, a 'positive' and a 'negative' pulses were acquired at each transmission angle to suppress tissue signal and enhance microbubble signal (Shen, et al. 2005). Fifty (50) pre- and 500 post-activation images were collected at a rate of 500 frames per second. A differential imaging technique is applied to remove the background signal (Brown, et al. 2017). Frames after activation were subtracted by the average of frames before activation to remove background signals. The region of interest (ROI) was defined by the bottom plane (indicated by the blue box between 16 to 17 mm in Figure 4) of the Opticell chamber where MDA-MB-231 breast cancer cells were attached. Customized Matlab scripts were written to enable all the analyses and calculations. All the images were shown in grey scale where each pixel in the image was normalized by the maximum pixel value.

Flow velocity mapping & Size estimation

After ultrasonic exposure of FR-nanodroplets, a portion of resultant microbubbles were still attached to the cells whereas another portion of large bubbles floated up due to buoyancy as illustrated in Figure 2.

The vaporized-nanodroplet (microbubble) rising velocity in the stagnant liquid is mainly governed by the buoyancy force and the drag force experienced by the vaporized nanodroplets. In the force balance approach, the rising velocity is calculated from the balance of buoyancy and drag force. The rising velocity of vaporized nanodroplets in a viscous liquid at low Reynolds number can be expressed by the equation (1) below:

$$V = \frac{(\rho_l - \rho_g) g D_b^2}{18 \mu_l} \qquad (1)$$

Calculations were adapted from Stokes' equation (Parmar and Majumder 2015) where V is the rising velocity, D_b is the diameter of microbubble, ρ_l is the density of liquid at 37 ºC (approximately 1 g/cm^3), ρ_g is the density of gas at 37 ºC (11.2 kg/m^3), g is the gravity acceleration (9.8 m/s^2) and μ_l is the viscosity of liquid at 37 ºC (8.90 × 10^{-3} dyne s/cm^2).

The size distribution of the attached vaporized nanodroplets can be directly estimated from microscopic images. Individual vaporized nanodroplets were segmented out of the images (T.J Atherton 1999) to estimate the diameter distribution of both vaporized FR- and NT-nanodroplets that remain attached to the cells. A customized Matlab script was written to perform the segmentation to separate the microbubbles out and measure their diameters. The size distribution of floating vaporized nanodroplets can be estimated by tracking average rising velocities of the newly vaporized nanodroplets immediately after acoustic activation using the flow velocity mapping technique described previously (Leow, et al. 2015) combined with Stokes' equation (Parmar and Majumder 2015). Briefly, the cross-correlation analysis was performed to compute a local velocity between the corresponding interrogation windows of two neighbouring ultrasound frames. A velocity map was displayed with color-coded velocity vectors. The full flow field within the

imaging plane of Opticell chamber was estimated and therefore flow velocity within any point in the imaging plane could be determined. The number of vectors and their locations in the image/video were chosen for visualization purpose. By estimating the average flow velocity in the resolution cell in all individual trials, the average size of bubble population could be obtained via Stokes' equation.

Figure 3 shows a representative flow velocity mapping of vaporized nanodroplets immediately after activation (supplementary video data 2). The movement of the vaporized nanodroplets could be visualized and the corresponding average flow velocity could be obtained. The average flow velocity obtained from flow velocity mapping was used for the size estimation combined with equation (1).

Statistical analysis

All data were expressed as the mean ± standard deviation. Statistical significances were analyzed using the two-sample Student's t-test (with the assumption of t-distribution) and two-sample z-test (with the assumption of normal distribution) according to the sample size. The Student's t-test was used to compare two sets of data with sample size smaller than 30 while the two-sample z-test was used to compare two sets of data with sample size larger than 30. A *p-value<0.05 was considered statistically significant, a **p-value<0.01 strongly significant, and a ***p-value<0.001 was highly significant.

RESULTS

Characterization of Nanodroplets

The size distribution of NT-nanodroplets and FR-nanodroplets measured using Nanoparticle Tracking Analysis (NTA) are illustrated in Figure 4. No statistically significant differences were found for the mean diameters of NT-nanodroplets and FR-nanodroplets (N=9). The mean diameters of NT-nanodroplets and FR-nanodroplets were 118.7±6.7 nm and 116.8±5.9 nm, respectively and

were within the size range for promoting EPR effect (up to 400 nm) demonstrated by the previous study (Ernsting, et al. 2013). The concentration of NT- and FR-nanodroplets were $(3.51\pm0.26)\times10^{10}$ droplets/mL and $(3.45\pm0.31)\times10^{10}$ droplets/mL respectively.

Acoustic response of vaporized nanodroplets

Figure 5 shows the temporal snapshots of FR and NT-nanodroplets in the Opticell chamber 0.002 s before, and 0.002 s and 1 s after activation (Supplementary video data 1). The bottom plane where the cells were located was between 16 and 17 mm. More persistent and visible ultrasound contrast signal could be seen for vaporised FR-nanodroplets compared to vaporised NT-nanodroplets 1 s after activation.

Figure 6 shows the quantitative analysis of acoustic response (i.e. the grayscale value) of vaporized FR- and NT- nanodroplets. First, the normalised contrast amplitude of FR-nanodroplets is significantly higher than the NT-nanodroplets. Secondly, it was observed that contrast signal of FR-nanodroplets was relatively persistent after activation, with 70% of the acoustic signals remaining 1s after activation, compared to the NT-nanodroplets where only 40% of the contrast signals remained. The fast decay of contrast signal from NT-nanodroplets could also be observed compared to the FR-nanodroplets.

Size comparison between floating and attached vaporized nanodroplets

Figure 7 shows the acquired microscopic images focused at the bottom of Opticell chamber before and after ultrasound exposure. Figure 8 shows the quantification of size distribution of both vaporized FR- and NT- nanodroplets attached to the cells. The number of vaporized FR-nanodroplets observed on the bottom plane was 6.3 times larger than that of vaporized NT-nanodroplets. The vaporized FR-nanodroplets had significantly larger diameters (mean=9.8 μm) compared to the vaporized NT-nanodroplets (mean=3.6 μm). Moreover, the vaporized attached FR-nanodroplets had a diameter distribution between 4 to 68 μm whereas the vaporized attached NT-

nanodroplets possessed a much narrower range (from 1 to 7 μm). Although there were some small vaporized NT-nanodroplets that could be seen, they were not adherent to the cells according to Figure 8.

The size distribution of attached vaporized nanodroplets were obtained using the microscope imaging and microbubble segmentation (Sennoga, et al. 2010) while the size distribution of floating vaporized nanodroplets were obtained using ultrasound imaging, flow velocity mapping and Stokes' theory. These two sets of data are shown in a box plot in Figure 9 for comparison. The mean diameter of FR- and NT- vaporized nanodroplets were 70 μm and 75 μm respectively. The maximum diameter estimated was approximately 150 μm. The average size of floating vaporized nanodroplets was significantly larger than that of cell-surface bound microbubbles generated in both cases. However, for the attached vaporized FR-nanodroplets, the maximum diameter of all microbubbles measured on the cell membrane was 68 μm as observed in Figure 7.

DISCUSSION

Targeted nanodroplets for molecular imaging has the potential of a wide range of clinical and pre-clinical applications in cancer and cardiovascular diseases (Marshalek, et al. 2016, Porter, et al. 2016). The study offers an improved understanding of the vaporization of the targeted nanodroplets in terms of their sizes and aoucstic response in comparison with non-targeted ones, taking advantage of high-frame-rate contrast-enhanced ultrasound and optical microscopy. Such understanding would help design optimized methodology for imaging and therapeutic applications. One potential quantity of interest is the surface density of the ligand of interest. This could potentially be achieved through quantifying the vaporized targeted droplets which currently will require further studies.

For imaging applications, the bioeffects induced after the activation of nanodroplets is required to be minimal for safety consideration. Any vaporized droplets with a diameter larger than, e.g. 10 microns, could cause occlusion in the microcirculation, and an increased risk of cavitation

induced bioeffects and should be avoided (Sheeran, et al. 2016). For therapeutic applications such as HIFU and histotripsy, the larger size of activated nanodroplets can facilitate cavitation to achieve better therapeutic performance (Moyer, et al. 2015, Vlaisavljevich, et al. 2017). Therefore, the size distribution of the nanodroplets is important for each specific applications.

Comparison with the existing literatures

The binding efficiency of the FR-nanodroplets in this study was about 2.4 activated nanodroplets per cell after activation according to the experimental results. For the size of targeted vaporized nanodroplets, Marshalek and coworkers also used the same nanodroplets to target the MDA-MB-231 breast cancer cells, however that work only focused on the size of the vaporized nanodroplets internalized within the cells rather than those attached to the cell surface (Marshalek, et al. 2016). Sheeran et al., 2013 used RGD targeted nanodroplets to target the HUVEC cells and their results show the size of vaporized targeted nanodroplets ranged from 1-3 μm (Sheeran, et al. 2013). In our study, a wide range of diameters (from 4 to 68 μm) of vaporized targeted nanodroplets could be observed by microscopic images. This could be due to the concentration used, the ultrasound pulse sequence employed and also different targeted ligands used. Future studies on such effects needs to be conducted. For the size of floating vaporized nanodroplets dislodged from cells, there is no previous literature reported on this topic to the best of our knowledge.

Different targeting ligands may have different affinities to the receptors on cells (Toporkiewicz, et al. 2015). If one targeting ligand has a very high affinity to the receptor, there will be more droplets attached on cells prior to activation. The high concentration of bubbles generated by ultrasound-mediated activation could likely lead to diffusion/coalescence on the membrane surface. However, the assumption was made that diffusion/coalescence could as well occur on the cell surface. Therefore, the size may also change due to different targeting ligands.

Acoustic response immediately after activation

There is a sharp decrease in the acoustic signal the first 100ms immediately following activation shown in Figure 5. This is likely because the large-sized newly vaporized nanodroplets float up to the top plane of the Opticell chamber when experiencing buoyant force. As vaporized nanodroplets moved away from the ROI as illustrated in Figure 5, there was a significant decrease in the acoustic signal. The populations of newly vaporized nanodroplets underwent some dynamic processes such as gas diffusion in/out of the microbubbles and the coalescence of microbubbles within the first 100ms (Lajoinie, et al. 2014, Raymond, et al. 2016). Moreover, the formation of the vortex due to the high MI activation pulse could also push the generated microbubbles out of the imaging plane as there was no confinement in the elevational direction in the Opticell chamber (Raymond, et al. 2016). The acoustic signal of newly vaporized NT-nanodroplets does not disappear at the end of 1 second post-activation. This is mainly because the NT-nanodroplets are subjected to non-specific binding to cells. It is feasible that the lipid component could possibly infuse into the cell membrane bilayers to contribute to the non-specific binding (Escribá, et al. 2008). Moreover, the acoustic signal decay may also be related to the cancer cell studied, the target ligand chosen (Marshalek, et al. 2016), the activation and imaging pulses (Sheeran, et al. 2013), and the confinement of experimental environment (Lin, et al. 2017) as the Opticell chamber is a confined environment.

Size distribution of attached vaporized nanodroplets

After activation, vaporized FR-nanodroplets were expected to remain on the bottom plane due to FR-binding to the cell membrane. While the successful binding and vaporization could be realized using nanodroplets, the maximum diameter of vaporized nanodroplets attached to the cells were as high as 68 μm which was larger than the mean diameter of the microbubble population before condensation (which has a peak size distribution centered approximately around 0.5 – 6 microns). The large FR-microbubbles (68 μm) were bound to the targeted cells despite the relatively large buoyant force. There are a few possible explanations for the large newly generated

microbubbles. First, from a chemistry perspective, the monolayer of the lipid shell will be zipped to form bilayer strands from the microbubble condensation to nanodroplets, followed by the bilayer strands being unzipped after activation to reform the monolayer (Mountford, et al. 2015, Sheeran, et al. 2016). The unstable vaporized nanodroplets may lack some lipids immediately after acoustic activation and subsequently may tend to coalesce to share more lipid shell to promote the formation of larger microbubbles. In addition, a larger activation energy barrier is required to achieve the homogenous nucleation of those nanodroplets of smaller diameters (less than 100nm) (Mountford, et al. 2015), thus that the nanodroplet size outliers (diameter larger than 1000nm) are easier to be activated to form larger vaporized nanodroplets. Second, from an imaging perspective, the high frame rate ultrasound imaging pulse from transducer may 'push' the microbubbles to coalesce to larger ones (Postema, et al. 2004). The secondary radiation force may also affect the microbubble coalescence as described in the literature (Antonios and James 2016, Himanshu, et al. 2017). Finally, from an activation perspective, although the activation frequency (8MHz) used in this study was higher than the activation frequency used in some previous studies (Sheeran, et al. 2016, Sheeran, et al. 2015), it may still not be high enough to completely vaporize all the nanodroplets, especially those which are small in size, due to the lack of a 'superharmonic focusing' effect which initiates the nanodroplet nucleation (Shpak, et al. 2014).

Moreover, the mean size of attached vaporized FR-nanodroplets was about 3 times larger than that of attached vaporized NT-nanodroplets. This may be because more FR-nanodroplets attached to the MDA-MB-231 cells than NT-nanodroplets prior to ultrasound activation. Thus, after activation, there were more vaporized FR-nanodroplets undergoing diffusion/coalescence to form larger microbubbles.

While the aggregation of nanodroplets once injected into the Opticell chamber cannot be absolutely rule out, the nanodroplet membranes do contain PEG which has a tendency to retard this phenomenon. Moreover, the aggregation of both kinds of nanodroplets was not observed under the microscope prior to activation as the resolution of the microscope is 0.1613 μm/pixel.

Spontaneous vaporization of nanodroplets

Spontaneous vaporisation of FR-nanodroplets could be seen before ultrasonic activation. This is due to the absorption of the thermal energy (temperature = 37 ºC) provided by the chamber environment. In this study, a high acoustic pressure (MI=1.9) activation pulse (with 10 half-cycles) was expected to destroy the existing spontaneously vaporized nanodroplets (William, et al. 2006) and also generate newly ultrasound-activated nanodroplets. Hence, most of the vaporized nanodroplets shown after ultrasound activation were expected to be the vaporized nanodroplets activated by the ultrasound pulse.

There were possible interactions between the spontaneously vaporized nanodroplets and nanodroplets under ultrasound. Thus, the presence of these spontaneously vaporized nanodroplets could have an influence on the activation process of the nanodroplets in their proximity by potentially assisting in the activation of nanodroplets.

It is possible that a small amount of spontaneously vaporized droplets would still persist after activation (attached/dislodged). However, since this will occur for both FR- and NT-experiments, the significant difference of size comparison was not expected to be affected.

A ‘no activation pulse’ control experiment was performed compared to an experiment with activation pulses and the results were shown in the Figure 10 below. As can be seen from the figure that the low-pressure imaging pulses were shown to not able to destroy any of the spontaneously vaporized droplets. For the experiment with imaging and activation pulses, as indicated by the red arrows on the figure, it can be clearly seen that the spontaneously vaporized droplets were destroyed by the activation pulses.

Flow velocity mapping

With respects to flow velocity mapping, it was difficult to associate the velocity vectors with individual vaporized nanodroplets due to the large resolution cell size which might contain a

number of vaporized nanodroplets. The signal amplitude within such a resolution cell is weighted by the individual bubble signal strengths which may be highly size dependent. Furthermore, it could be potentially affected by a number of elements, such as complex function of scattering, resonance and nonlinear detection scheme effects etc. However, we believe the size estimation approach used in this study is still able to demonstrate the average size range of the vaporized targeted droplets and help our understanding of their behavior after activation.

The imaging frequency used in this study was 4 MHz, which may not show well the small bubbles generated. The generated bubbles with approximately 2 μm may resonate at this imaging frequency according to a previous literature (Tang and Eckersley 2006).

Assumption of Stokes' equation

The Stokes' equation was used as a mathematical model to convert the rise velocity to the diameter of rising microbubbles (Parmar and Majumder 2015). There are three assumptions for applying this equation. First, it is assumed that the microbubbles are perfectly spherical. Second, it is assumed that there is no internal gas circulation within the microbubbles and no slip exists at the boundary. Third, it is assumed that the liquid inside the chamber is stagnant. In this study, the activation pulse may induce a flow inside the chamber. However, as can be seen from Figure 8, the flow was still dominated by the rising microbubbles. It may be possible that some non-gaseous particles may have detached from the bottom of Opticell chamber with the floating microbubbles, however, no non-gaseous attachment to the bubbles can be observed.

Size of nanodroplets before activation

The unfiltered (without size manipulation) FR- and NT-nanodroplets were used in this study. It is noted that the presence of nanodroplet size outliers may potentially affect the performance of acoustic vaporization of nanodroplets to give larger sizes of vaporized nanodroplets (Sheeran, et al. 2016). In the *in vivo* setting, the large vaporized nanodroplets should be filtered out by the lungs

(Butler and Hills 1979). Therefore, the size population of nanodroplets will need to be manipulated in future studies. Although the mean size of vaporized FR-nanodroplets generated immediately after activation is 9µm, vaporized droplet outliers as large as 68 µm were detected. The size population of newly generated microbubbles will also be affected by the gas concentrations in the ambient fluid and confined environment (Lin, et al. 2017).

MDA-MB-231 breast cancer cells

The MDA-MB-231 cells are immortalized, having gone through a number of passages. This large number of passages could result in cell receptor heterogeneity, thus different number of receptors. While this has not been studied in detail, Marshalek et al. (Marshalek, et al. 2016) alluded to efficiency of binding to MDA-MB-231 using folate-targeted nanodroplets. This has also been noted for other cell lines (i.e. Pancreatic Cancer [Panc]-1). Whether this is due to cell contact/confluence or large number of passages generating heterogeneity, is not explicitly known.

Ultrasound pulses on detachment

It has been shown that ultrasound pulses with even medium amplitude are able to detach targeted microbubbles (Loughran, et al. 2012). Unlike imaging vascular endothelial targets where shear stress from blood flow can detach the microbubbles from their bound sites, reducing ultrasound signal, the flow is very limited outside the vasculature and any detached bubbles could potentially stay in position and continue to contribute to ultrasound signal. The activation pulse could also cause diffusion of gas out of the microbubbles resulting in loss of echogenicity. Future work is required to study the impact of potential detachment of vaporized nanodroplets on the ultrasound molecular images.

CONCLUSION

In summary, we have investigated binding of targeted nanodroplets to MDA-MB-231 breast cancer cells as well as the acoustic response and size distribution of newly generated attached microbubbles immediately after activation. It is found that the size of floating microbubbles is on average more than 7 times larger than the size of targeted microbubbles to the cells. The results show the acoustic signal of generated FR-microbubbles is persistent after activation, with 70% acoustic signals remaining 1 second after activation, compared to the NT-microbubbles where only 40% of the acoustic signal remains. The microscopic imaging shows on average 6 times more FR-microbubbles generated with wider range of diameters (from 4 to 68μm) attach to the cells compared to NT-microbubbles (from 1 to 7 μm) with non-specific binding after activation. It is also found that the mean size of attached vaporized FR-nanodroplets is about 3 times larger than that of attached vaporized NT-nanodroplets. This investigation and quantification provides a better understanding of the acoustic response and size distribution of these vaporized targeted nanodroplets for future ultrasound molecular imaging and therapeutic studies.

ACKNOWLEDGEMENTS

This research was partially funded by the UK EPSRC under Grant Nos. EP/N015487/1, EP/N014855/1, and EP/ M011933/1, and the CRUK Multidisciplinary Project Award (No. C53470/A22353).

REFERENCES

Antonios NP, James JC. Superharmonic microbubble Doppler effect in ultrasound therapy. Physics in Medicine & Biology 2016; 61:6154.

Aydin O, Vlaisavljevich E, Yuksel Durmaz Y, Xu Z, ElSayed ME. Noninvasive Ablation of Prostate Cancer Spheroids Using Acoustically-Activated Nanodroplets. Mol Pharm 2016; 13:4054-65.

Brown J, Christensen-Jeffries K, Harput S, Dunsby C, Tang MX, Eckersley RJ. 2017 Investigation of microbubble detection methods for super-resolution imaging of microvasculature. *2017 IEEE International Ultrasonics Symposium (IUS)*, 1-4.

Butler BD, Hills BA. The lung as a filter for microbubbles. Journal of Applied Physiology 1979; 47:537-43.

Chen C, Ke J, Zhou XE, Yi W, Brunzelle JS, Li J, Yong EL, Xu HE, Melcher K. Structural basis for molecular recognition of folic acid by folate receptors. Nature 2013; 500:486-9.

Dijkmans PA, Juffermans LJM, Musters RJP, van Wamel A, ten Cate FJ, van Gilst W, Visser CA, de Jong N, Kamp O. Microbubbles and ultrasound: from diagnosis to therapy. European Journal of Echocardiography 2004; 5:245-46.

Eckersley RJ, Chin CT, Burns PN. Optimising phase and amplitude modulation schemes for imaging microbubble contrast agents at low acoustic power. Ultrasound in Medicine & Biology 2005; 31:213-19.

Ernsting MJ, Murakami M, Roy A, Li S-D. Factors controlling the pharmacokinetics, biodistribution and intratumoral penetration of nanoparticles. Journal of Controlled Release 2013; 172:782-94.

Escribá PV, González-Ros JM, Goñi FM, Kinnunen PKJ, Vigh L, Sánchez-Magraner L, Fernández AM, Busquets X, Horváth I, Barceló-Coblijn G. Membranes: a meeting point for lipids, proteins and therapies. Journal of Cellular and Molecular Medicine 2008; 12:829-75.

Hadinger KP, Marshalek JP, Sheeran PS, Dayton PA, Matsunaga TO. Optimization of Phase-Change Contrast Agents for Targeting MDA-MB-231 Breast Cancer Cells. Ultrasound in Medicine & Biology 2018; 44:2728-38.

Himanshu S, Kenneth BB, Shenwen H, Tao P, Shaoling H, David DM, Christy KH. In vitro thrombolytic efficacy of echogenic liposomes loaded with tissue plasminogen activator and octafluoropropane gas. Physics in Medicine & Biology 2017; 62:517.

Ji T, Zhao Y, Ding Y, Nie G. Using functional nanomaterials to target and regulate the tumor microenvironment: diagnostic and therapeutic applications. Advanced Materials 2013; 25:3508-25.

Kasoji SK, Pattenden SG, Malc EP, Jayakody CN, Tsuruta JK, Mieczkowski PA, Janzen WP, Dayton PA. Cavitation Enhancing Nanodroplets Mediate Efficient DNA Fragmentation in a Bench Top Ultrasonic Water Bath. PLoS One 2015; 10:e0133014.

Kim U, Shu C-W, Dane KY, Daugherty PS, Wang JYJ, Soh HT. Selection of mammalian cells based on their cell-cycle phase using dielectrophoresis. Proceedings of the National Academy of Sciences of the United States of America 2007; 104:20708-12.

Kripfgans OD, Fowlkes JB, Miller DL, Eldevik OP, Carson PL. Acoustic droplet vaporization for therapeutic and diagnostic applications. Ultrasound in Medicine & Biology 2000; 26:1177-89.

Lajoinie G, Gelderblom E, Chlon C, Bohmer M, Steenbergen W, de Jong N, Manohar S, Versluis M. Ultrafast vapourization dynamics of laser-activated polymeric microcapsules. Nat Commun 2014; 5:3671.

Leow CH, Bazigou E, Eckersley RJ, Alfred C, Weinberg PD, Tang M-X. Flow velocity mapping using contrast enhanced high-frame-rate plane wave ultrasound and image tracking: Methods and initial in vitro and in vivo evaluation. Ultrasound in medicine & biology 2015; 41:2913-25.

Lin S, Shah A, Hernández-Gil J, Stanziola A, Harriss BI, Matsunaga TO, Long N, Bamber J, Tang M-X. Optically and acoustically triggerable sub-micron phase-change contrast agents for enhanced photoacoustic and ultrasound imaging. Photoacoustics 2017; 6:26-36.

Lin S, Zhang G, Leow CH, Matsunaga OT, Tang MX. 2016 Vaporising phase change ultrasound contrast agent in microvascular confinement. *2016 IEEE International Ultrasonics Symposium (IUS)*, 1-4.

Lin S, Zhang G, Leow CH, Tang M-X. Effects of microchannel confinement on acoustic vaporisation of ultrasound phase change contrast agents. Physics in Medicine & Biology 2017; 62:6884.

Lin S, Zhang G, Leow CH, Tang MX. Effects of microchannel confinement on acoustic vaporisation of ultrasound phase change contrast agents. Physics in Medicine & Biology 2017; 62:6884.

Liu WW, Liu SW, Liou YR, Wu YH, Yang YC, Wang CR, Li PC. Nanodroplet-Vaporization-Assisted Sonoporation for Highly Effective Delivery of Photothermal Treatment. Sci Rep 2016; 6:24753.

Loughran J, Sennoga C, R JE, Tang MX. Effect of ultrasound on adherent microbubble contrast agents. Phys Med Biol 2012; 57:6999-7014.

Marshalek JP, Sheeran PS, Ingram P, Dayton PA, Witte RS, Matsunaga TO. Intracellular delivery and ultrasonic activation of folate receptor-targeted phase-change contrast agents in breast cancer cells in vitro. J Control Release 2016; 243:69-77.

Matsunaga TO, Sheeran PS, Luois S, Streeter JE, Mullin LB, Banerjee B, Dayton PA. Phase-change nanoparticles using highly volatile perfluorocarbons: toward a platform for extravascular ultrasound imaging. Theranostics 2012; 2:1185-98.

Mercado KP, Radhakrishnan K, Stewart K, Snider L, Ryan D, Haworth KJ. Size-isolation of ultrasound-mediated phase change perfluorocarbon droplets using differential centrifugation. The Journal of the Acoustical Society of America 2016; 139:EL142-EL48.

Moncion A, Arlotta KJ, Kripfgans OD, Fowlkes JB, Carson PL, Putnam AJ, Franceschi RT, Fabiilli ML. Design and Characterization of Fibrin-Based Acoustically Responsive Scaffolds for Tissue Engineering Applications. Ultrasound Med Biol 2016; 42:257-71.

Montaldo G, Tanter M, Bercoff J, Benech N, Fink M. Coherent plane-wave compounding for very high frame rate ultrasonography and transient elastography. IEEE Trans Ultrason Ferroelectr Freq Control 2009; 56:489-506.

Morris RT, Joyrich RN, Naumann RW, Shah NP, Maurer AH, Strauss HW, Uszler JM, Symanowski JT, Ellis PR, Harb WA. Phase II study of treatment of advanced ovarian cancer with folate-receptor-targeted therapeutic (vintafolide) and companion SPECT-based imaging agent (99mTc-etarfolatide)†. Annals of Oncology 2014; 25:852-58.

Mountford PA, Thomas AN, Borden MA. Thermal Activation of Superheated Lipid-Coated Perfluorocarbon Drops. Langmuir 2015; 31:4627-34.

Moyer LC, Timbie KF, Sheeran PS, Price RJ, Miller GW, Dayton PA. High-intensity focused ultrasound ablation enhancement in vivo via phase-shift nanodroplets compared to microbubbles. J Ther Ultrasound 2015; 3:7.

Nakamura Y, Mochida A, Choyke PL, Kobayashi H. Nanodrug Delivery: Is the Enhanced Permeability and Retention Effect Sufficient for Curing Cancer? Bioconjugate Chemistry 2016; 27:2225-38.

Naumann RW, Coleman RL, Burger RA, Sausville EA, Kutarska E, Ghamande SA, Gabrail NY, DePasquale SE, Nowara E, Gilbert L, Gersh RH, Teneriello MG, Harb WA, Konstantinopoulos PA, Penson RT, Symanowski JT, Lovejoy CD, Leamon CP, Morgenstern DE, Messmann RA. PRECEDENT: A Randomized Phase II Trial Comparing Vintafolide (EC145) and Pegylated Liposomal Doxorubicin (PLD) in Combination Versus PLD Alone in Patients With Platinum-Resistant Ovarian Cancer. Journal of Clinical Oncology 2013; 31:4400-06.

Oleksandr S, Laura S, Michel V, Detlef L. The role of gas in ultrasonically driven vapor bubble growth. Physics in Medicine & Biology 2013; 58:2523.

Parker N, Turk MJ, Westrick E, Lewis JD, Low PS, Leamon CP. Folate receptor expression in carcinomas and normal tissues determined by a quantitative radioligand binding assay. Analytical Biochemistry 2005; 338:284-93.

Parmar R, Majumder SK. Terminal rise velocity, size distribution and stability of microbubble suspension. Asia-Pacific Journal of Chemical Engineering 2015; 10:450-65.

Porter TR, Arena C, Sayyed S, Lof J, High RR, Xie F, Dayton PA. Targeted Transthoracic Acoustic Activation of Systemically Administered Nanodroplets to Detect Myocardial Perfusion Abnormalities. Circ Cardiovasc Imaging 2016; 9.

Postema M, Marmottant P, Lancée CT, Hilgenfeldt S, Jong Nd. Ultrasound-induced microbubble coalescence. Ultrasound in Medicine & Biology 2004; 30:1337-44.

Raymond JL, Luan Y, Peng T, Huang SL, McPherson DD, Versluis M, de Jong N, Holland CK. Loss of gas from echogenic liposomes exposed to pulsed ultrasound. Phys Med Biol 2016; 61:8321-39.

Sennoga CA, Mahue V, Loughran J, Casey J, Seddon JM, Tang M, Eckersley RJ. On Sizing and Counting of Microbubbles Using Optical Microscopy. Ultrasound in Medicine & Biology 2010; 36:2093-96.

Sheeran PS, Daghighi Y, Yoo K, Williams R, Cherin E, Foster FS, Burns PN. Image-Guided Ultrasound Characterization of Volatile Sub-Micron Phase-Shift Droplets in the 20–40 MHz Frequency Range. Ultrasound in Medicine & Biology 2016; 42:795-807.

Sheeran PS, Dayton PA. Improving the performance of phase-change perfluorocarbon droplets for medical ultrasonography: current progress, challenges, and prospects. Scientifica (Cairo) 2014; 2014:579684.

Sheeran PS, Matsuura N, Borden MA, Williams R, Matsunaga TO, Burns PN, Dayton PA. Methods of Generating Sub-Micron Phase-Shift Perfluorocarbon Droplets for Applications in Medical Ultrasonography. IEEE Trans Ultrason Ferroelectr Freq Control 2016.

Sheeran PS, Rojas JD, Puett C, Hjelmquist J, Arena CB, Dayton PA. Contrast-enhanced ultrasound imaging and in vivo circulatory kinetics with low-boiling-point nanoscale phase-change perfluorocarbon agents. Ultrasound Med Biol 2015; 41:814-31.

Sheeran PS, Streeter JE, Mullin LB, Matsunaga TO, Dayton PA. Toward ultrasound molecular imaging with phase-change contrast agents: an in vitro proof of principle. Ultrasound Med Biol 2013; 39:893-902.

Sheeran PS, Wong VP, Luois S, McFarland RJ, Ross WD, Feingold S, Matsunaga TO, Dayton PA. Decafluorobutane as a Phase-Change Contrast Agent for Low-Energy Extravascular Ultrasonic Imaging. Ultrasound in Medicine and Biology 2011; 37:1518-30.

Shen C-C, Chou Y-H, Li P-C. Pulse Inversion Techniques in Ultrasonic Nonlinear Imaging. Journal of Medical Ultrasound 2005; 13:3-17.

Shpak O, Verweij M, Vos HJ, de Jong N, Lohse D, Versluis M. Acoustic droplet vaporization is initiated by superharmonic focusing. Proc Natl Acad Sci U S A 2014; 111:1697-702.

Tang Mx, Eckersley RJ. Nonlinear propagation of ultrasound through microbubble contrast agents and implications for imaging. IEEE Transactions on Ultrasonics, Ferroelectrics, and Frequency Control 2006; 53:2406-15.

Toporkiewicz M, Meissner J, Matusewicz L, Czogalla A, Sikorski AF. Toward a magic or imaginary bullet? Ligands for drug targeting to cancer cells: principles, hopes, and challenges. International journal of nanomedicine 2015; 10:1399-414.

Tremblay-Darveau C, Williams R, Milot L, Bruce M, Burns PN. Combined perfusion and doppler imaging using plane-wave nonlinear detection and microbubble contrast agents. IEEE Transactions on Ultrasonics, Ferroelectrics, and Frequency Control 2014; 61:1988-2000.

Vlaisavljevich E, Owens G, Lundt J, Teofilovic D, Ives K, Duryea A, Bertolina J, Welling TH, Xu Z. Non-Invasive Liver Ablation Using Histotripsy: Preclinical Safety Study in an In Vivo Porcine Model. Ultrasound Med Biol 2017; 43:1237-51.

William TS, Flemming F, Priya V, Audun T, Jonny Ø, Barry BG. The influence of acoustic transmit parameters on the destruction of contrast microbubbles in vitro. Physics in Medicine & Biology 2006; 51:4031.

Winnard PT, Jr., Pathak AP, Dhara S, Cho SY, Raman V, Pomper MG. Molecular imaging of metastatic potential. Journal of nuclear medicine : official publication, Society of Nuclear Medicine 2008; 49 Suppl 2:96S-112S.

Zhang G, Harput S, Hu H, Christensen-Jeffries K, Zhu J, Brown J, Dunsby C, R JE, Tang M. 2018 Fast Acoustic Wave Sparsely Activated Localization Microscopy (fast-AWSALM) using Octafluoropropane Nanodroplets. *2018 IEEE International Ultrasonics Symposium (IUS)*, 1-4.

Zhang G, Harput S, Lin S, Christensen-Jeffries K, Leow CH, Brown J, Dunsby C, Eckersley RJ, Tang M-X. Acoustic wave sparsely activated localization microscopy (AWSALM): Super-resolution ultrasound imaging using acoustic activation and deactivation of nanodroplets. Applied Physics Letters 2018; 113:014101.

Zhang G, Harput S, Lin S, Leow CH, Christensen-Jeffries K, Brown J, Dunsby C, Eckersley RJ, Tang MX. 2018 Super-Localisation Ultrasound Imaging using Sparse Activation of Low-Boiling-Point Nanodroplets. *The 23rd European Symposium on Ultrasound Contrast Imaging*. Rotterdam, Netherlands, 171-74.

Zhang G, Lin S, Leow CH, Pang K, Hernández-Gil J, Chee M, Long NJ, Matsunaga TO, Tang MX. 2017 Acoustic response of targeted nanodroplets post-activation using high frame rate imaging. *2017 IEEE International Ultrasonics Symposium (IUS)*, 1-4.

Zhou QL, Chen ZY, Wang YX, Yang F, Lin Y, Liao YY. Ultrasound-mediated local drug and gene delivery using nanocarriers. Biomed Res Int 2014; 2014:963891.

Zhu D, Wu S, Hu C, Chen Z, Wang H, Fan F, Qin Y, Wang C, Sun H, Leng X, Kong D, Zhang L. Folate-targeted polymersomes loaded with both paclitaxel and doxorubicin for the combination chemotherapy of hepatocellular carcinoma. Acta Biomater 2017.

Figures

Figure. 1. Schematic diagram of the experimental set-up (not to scale). The red box indicates the region of interest of ultrasound images at the upper and lower planes (MDA-MB-231 breast cancer cells) of the Opticell chamber.

Figure. 2. Schematic diagram shows the cross section of Opticell chamber after acoustic activation of FR-nanodroplets. A portion of newly vaporized FR-nanodroplets were still attached to breast cancer cells whereas another portion of large vaporized FR-nanodroplets were floating.

Figure. 3. The concentration and size characterization of NT- and FR-nanodroplets measured using Nanoparticle Tracking Analysis (NTA) (N=9). The curve and its corresponding shaded error bar represent the mean and standard deviation respectively. NT-nanodroplets: 118.7±6.7 nm and FR-nanodroplets: 116.8±5.9 nm.

Figure. 4. Representative temporal snapshots show FR- and NT-nanodroplets in Opticell chamber 0.002s before, and 0.002s and 1s after activation respectively using the pulse inversion imaging at MI=0.1 and

focus-pulse activating at MI=1.9. The region of interest (ROI) shows the top plane (indicated by the red box between 14 to 15 mm) and bottom plane (indicated by the blue box between 16 to 17 mm) of the Opticell chamber where MDA-MB-231 breast cancer cells located.

Figure. 5. Quantification of normalized acoustic amplitude (i.e. the grayscale value of pixels in ROI) of activation of FR- and NT-nanodroplets within bottom ROIs in the Opticell chambers using the pulse inversion imaging at MI=0.1 and focus-pulse activating at MI=1.9. The blue curve represents for FR-nanodroplet and the red curve represents for NT-nanodroplet. The shaded error bar represents the corresponding standard deviation.

Figure. 6. Representative microscopic imaging of FR-nanodorplets and NT-nanodroplets before and after activation in Opticell chamber. (a) FR-nanodroplets before activation (b) FR-nanodroplets after activation (c) NT-nanodroplets before activation (d) NT-nanodroplets after activation. The scale bar represent 30 μm.

Figure. 7. The histogram (a) and box plot (b) shows the diameter distribution of both vaporized FR- (N=819) and NT- (N=139) nanodroplets (NDs) immediately after acoustic activation of nanodroplets. The newly vaporised FR-nanodroplets have a wider range of diameters than vaporized NT-nanodroplets. The mean diameter of vaporized FR-nanodroplets is significantly larger than that of vaporized NT-nanodroplets.

Figure. 8. Quantitative flow vector visualization of vaporized FR-nanodroplets generated immediately after activation inside the Opticell chamber. Each measurement is averaged over 10 ms to reduce the noise. The data used is after the processing of singular value decomposition filtering to reduce the noise. The length and direction of the vector arrow represent the magnitude and direction of the velocity within the region of the arrow. Supplementary video illustrates the temporal changes of flow patterns in the Opticell chamber.

Figure. 9. The box plot shows the size distribution of floating and attached FR- and NT- vaporized nanodroplets (NDs) immediately after acoustic activation (v = vaporized). The sizes of attached, vaporized nanodroplets were obtained from microscopic imaging. Alternatively, the sizes of floating vaporized nanodroplets were obtained from flow velocity mapping of ultrasound imaging. As can be seen from the figure, the size of floating vaporized nanodroplets were significantly larger than that of attached vaporized nanodroplets for both vaporized FR- and NT- nanodroplets. *** represent highly significant difference, p-value<0.001.

Figure. 10. A control experiment with only imaging pulses (left) and an experiment with both imaging and activation pulses (right) were performed at 37 degrees in a droplet solution, demonstrating that the activation pulse was able to remove the spontaneously vaporized droplets. (a) and (c) show two consecutive imaging frame without activation pulses. (b) and (d) show two consecutive imaging frame (before and after activation respectively) with activation pulses in between. The experimental conditions were kept the same as detailed in Table 1. Note that (a) and (b) are very first frame of the individual experiment showing spontaneously vaporized droplets, while the horizontal line in (d) corresponds to the ultrasound focal depth of the vaporization pulses.

Tables.

Table 1. Imaging-Activation-Imaging sequence and the corresponding ultrasound parameters used in the experiments. PNP represents the spatial and temporal peak-negative-pressure.

State	Pulse type	Transmit frequency (MHz)	Pulse length (half-cycle)	PNP (MPa)	Mechanical Index
Imaging (Before)	Plane-wave	4	1	0.20	0.10
Activation	Focus-wave	8	10	5.37	1.90
Imaging (After)	Plane-wave	4	1	0.20	0.10

Figure 1.

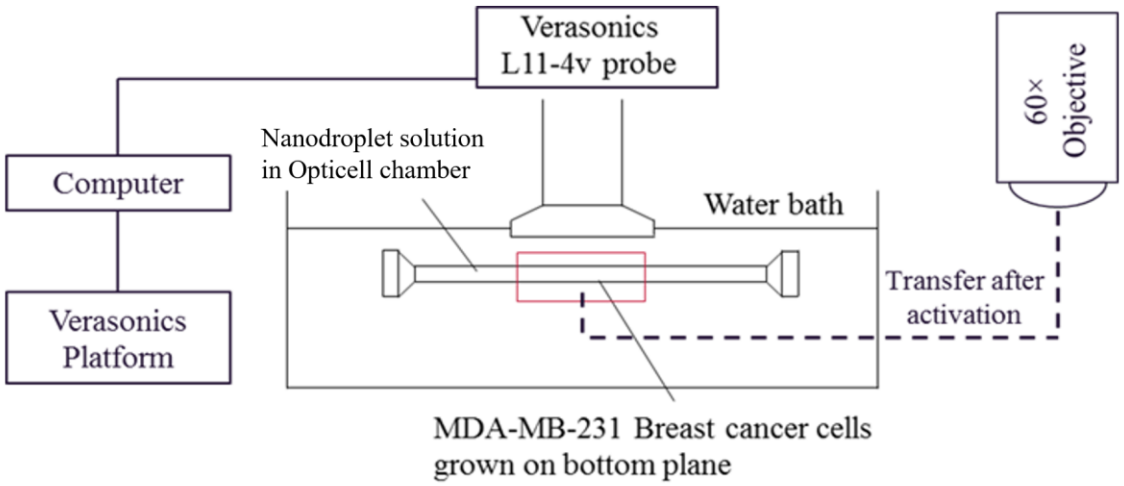

Figure 2.

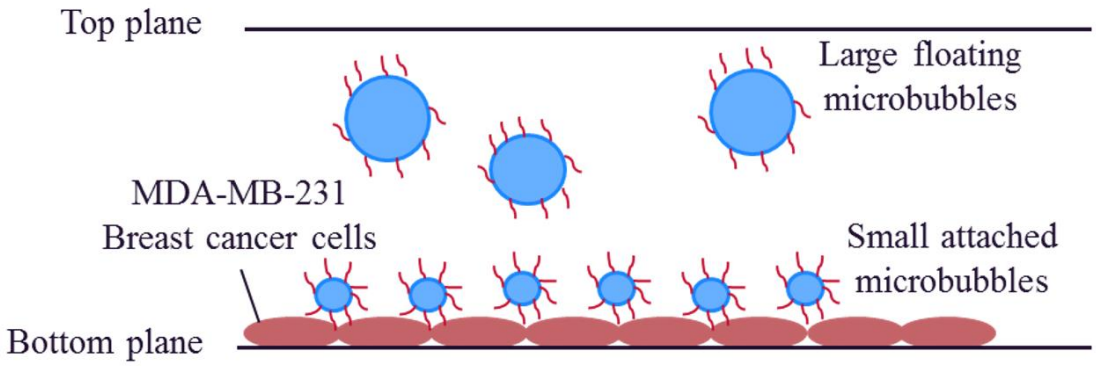

Figure 3.

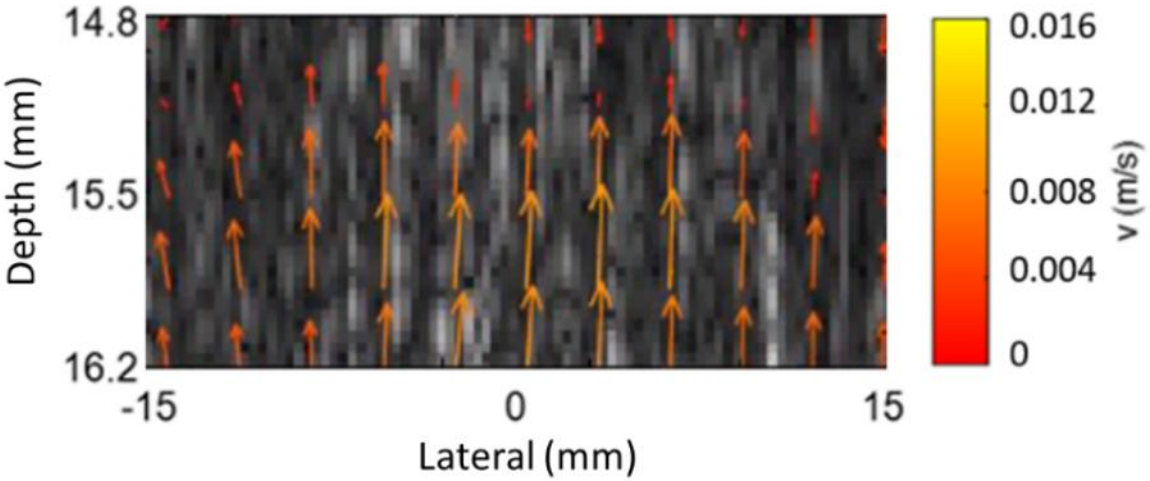

Figure 4.

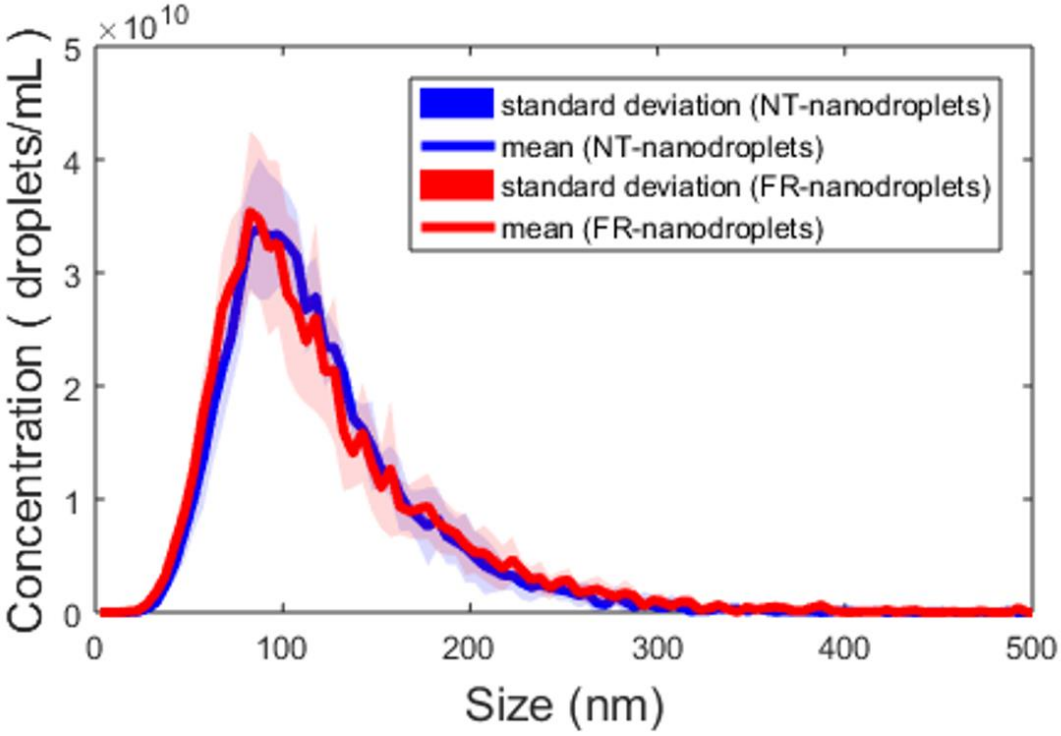
×10^10
5
4
3
2
1
0
Concentration (droplets/mL)
0
100
200
300
400
500
Size (nm)
standard deviation (NT-nanodroplets)
mean (NT-nanodroplets)
standard deviation (FR-nanodroplets)
mean (FR-nanodroplets)

1

2 Figure 5.

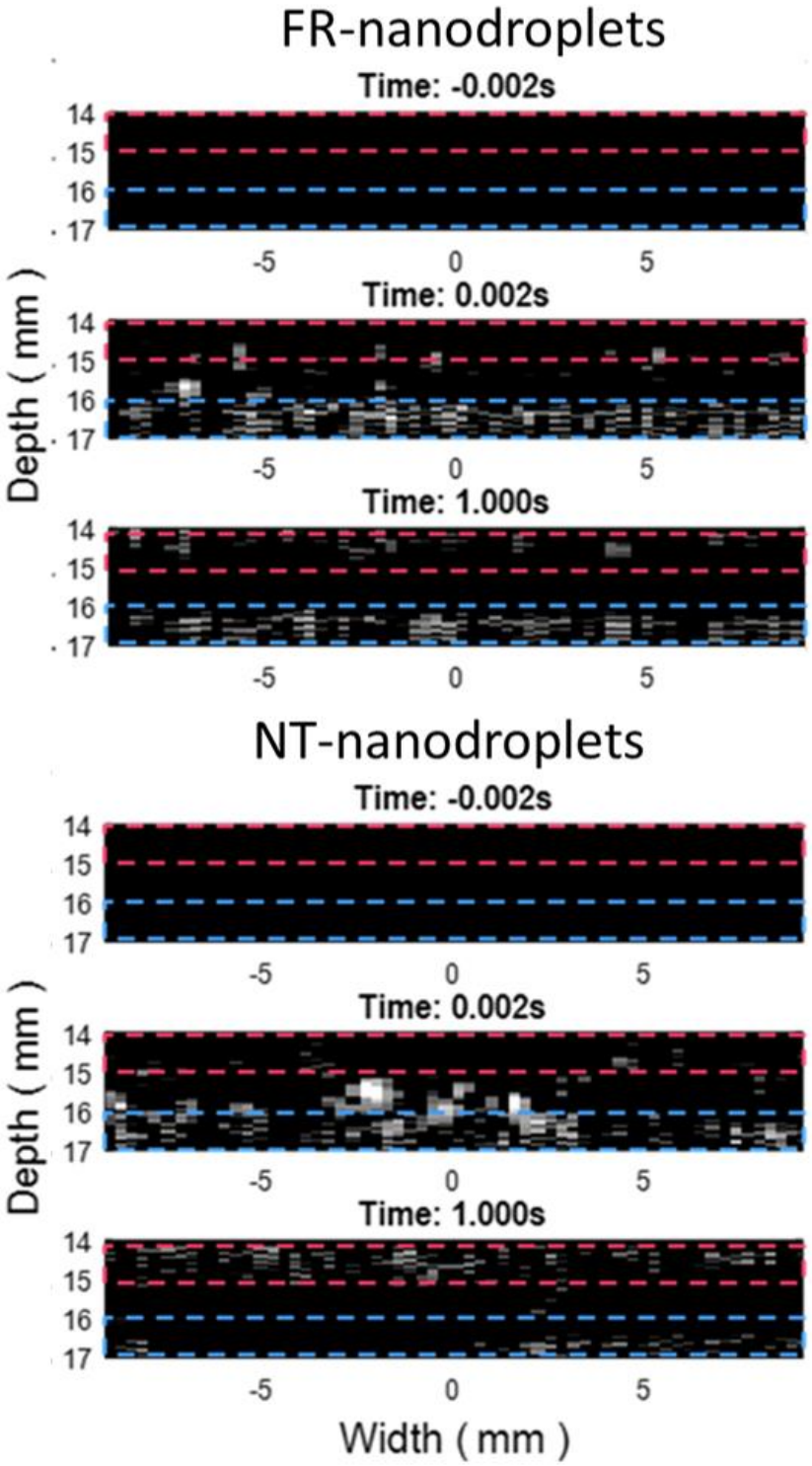
FR-nanodroplets
Time: -0.002s
Time: 0.002s
Time: 1.000s
NT-nanodroplets
Time: -0.002s
Time: 0.002s
Time: 1.000s
Depth (mm)
Width (mm)
14
15
16
17
-5
0
5

1

2 Figure 6.

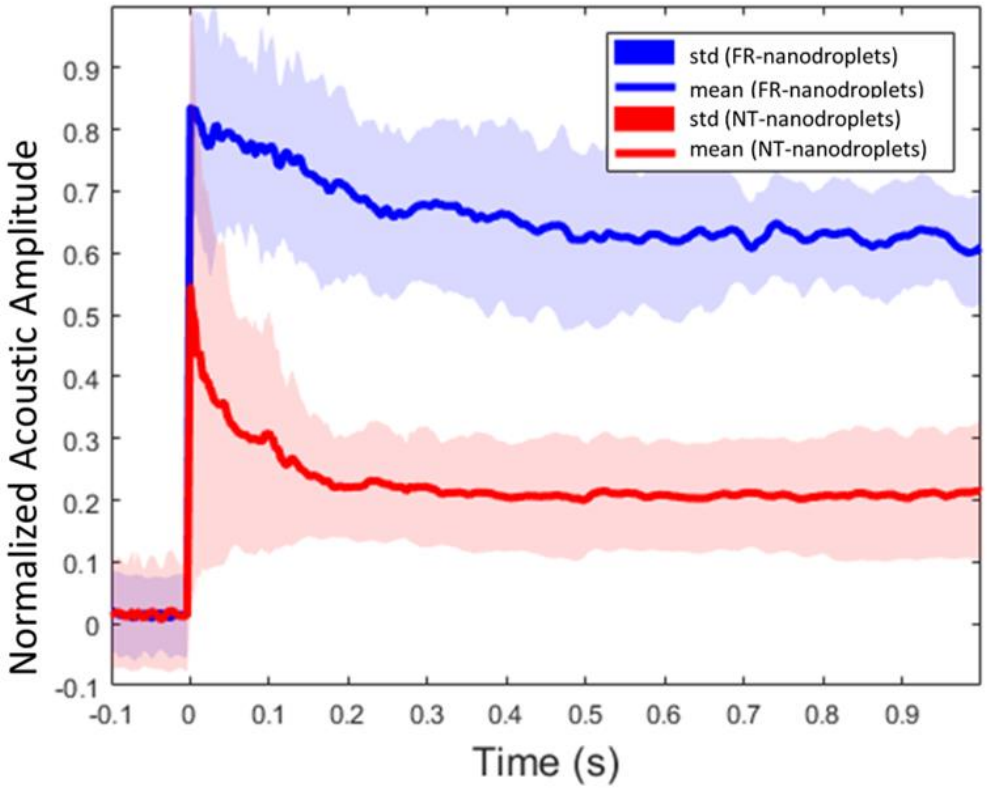

1

2 Figure 7.

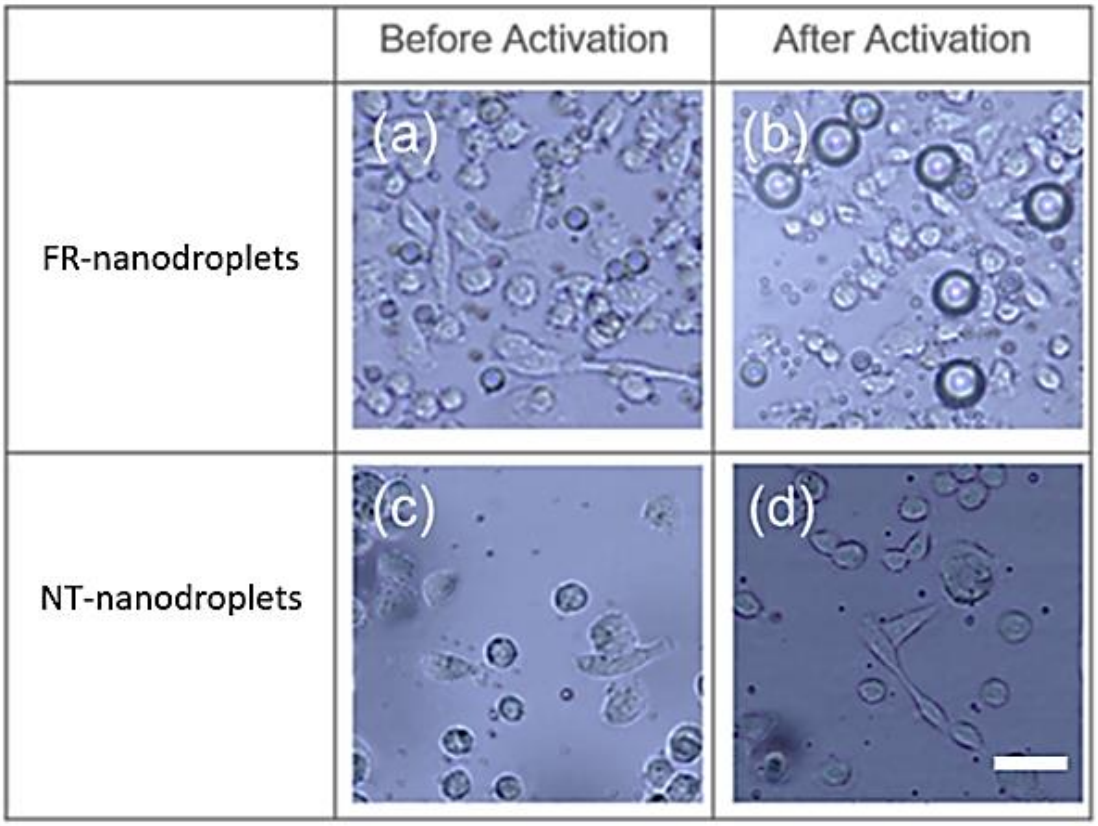

3

4 Figure 8.

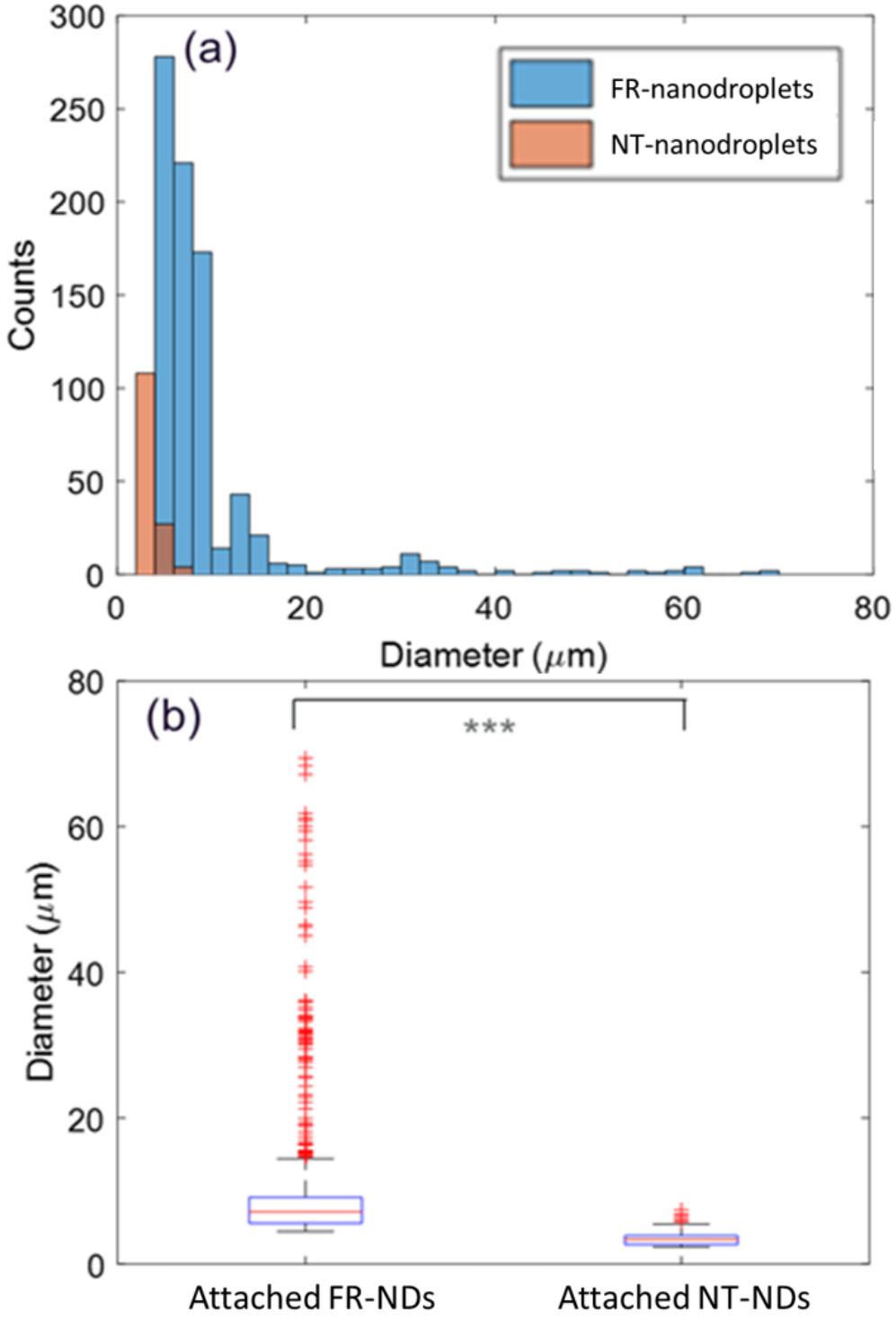
(a)
FR-nanodroplets
NT-nanodroplets
Counts
Diameter (μm)
(b)
***
Diameter (μm)
Attached FR-NDs
Attached NT-NDs

1

2 Figure 9.

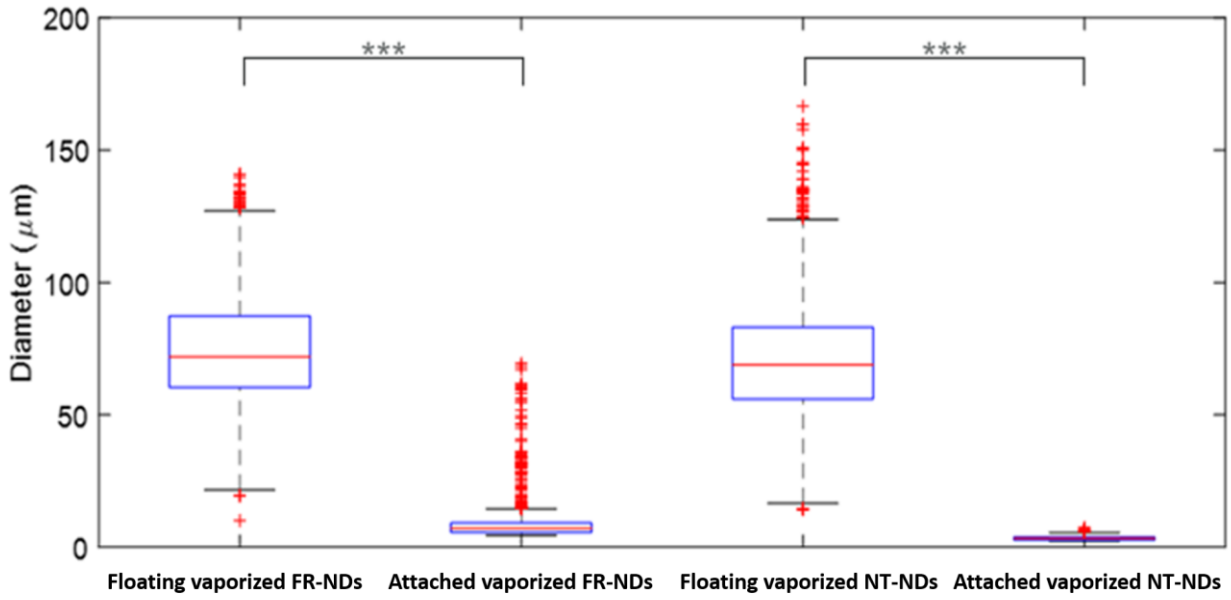

1

2 Figure 10.

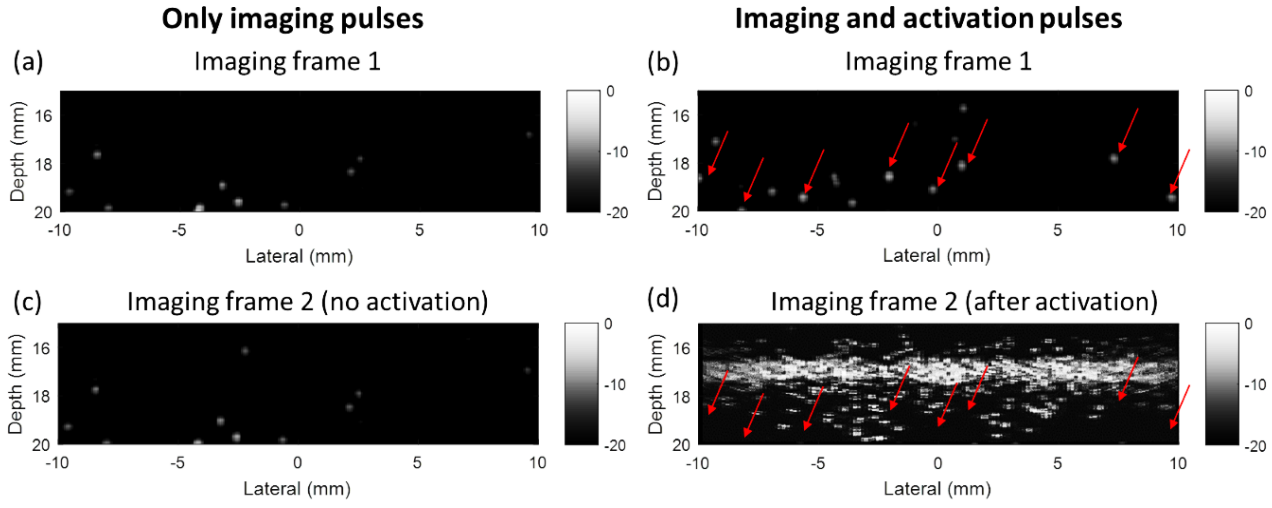

3